Innovative Systems Design and Engineering
ISSN 2222-1727 (Paper) ISSN 2222-2871 (Online)
Vol.6, No.5, 2015

Numerical Study of Scan Speed Selection and Kerf Depth Prediction in Silicon Laser Machining

Titus Mulembo[1*] B. W. Ikua[1] J. N. Keraita[2] A. Niyibizi[2] C. Kagiri[1]
1.Mechatronic Engineering Department, JKUAT, P.O Box 62000, Nairobi-Kenya
2.Dedan Kimathi University of Technology, P.O Box 657, 10100, Nyeri-Kenya

Abstract
In recent times, lasers have gained popularity in machining applications. This trend has been due to the various unique properties that lasers posses. These properties include the ease of manipulation, and the ability to focus the beam to a small spot. Laser machining offers a better alternative to traditional machining since it does cause tool wear, and no mechanical cutting force is required. In this research, effects of the Nd:YAG laser scan speed on kerf depth is investigated. A numerical model was developed using finite element analysis method to investigate the effects using COMSOL^R. ImageJ^R software was used for image analysis and generation of kerf depth predictions. The results of this study show that increasing the laser scan speed led to a decrease in the kerf depth. Various scan speeds can also be optimally selected for different laser application. Cutting quality is improved if scan speeds of the laser are chosen properly.
Keywords: Scan speed, kerf depth, laser.

1. Introduction

Laser machining of silicon material is currently applied in micromachining in the micrometer range, in the manufacture of different Micro Electro-Mechanical Systems and Micro Opto-Electro Mechanical Systems. Monocrystalline silicon has applications in microelectronic chips and solar panels because of its excellent properties. This properties include large absorptance and low convection heat transfer coefficient (Brandi et al. 2010).

This research sought to model monocrystalline silicon behavior during Nd:YAG laser micromachining to develop an understanding of the heat affected zones. It also sought to optimize the process parameter that is, scan speed. The relationship between various cutting speeds and the outputs need to be established so that they can be controlled during machining to attain desirable outcomes.

Modeling methods are useful as they reduce cost involved in mounting experiments. They also help bring out process information relating to conditions for improved accuracy, consistency and predictability in a cost effective way. Experiments are, however, useful as they demonstrate the actual performance of devices. They are therefore used to validate models (Yilbas 2004).

Mazumder and Steen (1980) developed a three dimensional model of laser materials processing with a moving Gaussian heat source using finite difference numerical technique. This model was used to predict temperature profile, maximum processing speed and heat affected zone in the region of laser-surface interaction. Modest (1993) put forward a three-dimensional transient ablation model for laser machining ceramics to predict transient temperature distribution and groove shape. Finite difference method was used to solve the three dimensional conduction equations.

Treatment of laser processing using finite element was demonstrated by Yu (1997), who developed a model which incorporated boundary and loading conditions, as well as phase changes in the laser cutting process. Yu used the ANSYS^R Parametric Design Language and showed that the numerical method compared well with experimentally obtained.

From the literature, it can be seen that research work in the area of laser machining of silicon is ongoing and that considerable progress has been made. This paper's aim was to provide a model for laser cutting, taking into account the effect of laser light absorption within the silicon, temperature changes within the silicon. The model will also help to evaluate the influence of the laser scan speed on kerf depths, and how it can facilitate cutting speed selection. The results of this study show that increasing the laser scan speed led to a decrease in the kerf depth.

2. Mathematical Formulation

Below is a brief description of how the mathematical formulations were carried out.

2.1 Physical M

odel can also be used to obtain the same accuracy on all the points of the model. However, it would greatly increase the computing time without significantly affecting the result.

The major assumptions on which the model is based are as follows:

1. Thermophysical properties are constant and uniform.
2. The laser beam has a Gaussian distribution in pulsed mode.

3. The plasma formed, if any, is transparent and inert to the laser flux density and is thereby neglected. As a consequence, non-thermal photo-chemical ablation is also ignored.
4. The laser beam operates in the fundamental Transverse Electromagnetic Mode (TEM_{00}). The beam divergence angle is small and the beam is focused intensely. Incident laser energy is also directional and collimated.
5. The material is assumed to be isotropic, homogeneous, and linear elastic.

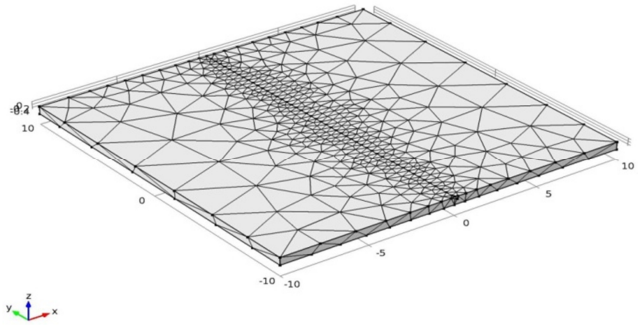

Figure 1(a). Coarse mesh as generated by the COMSOL^R software.

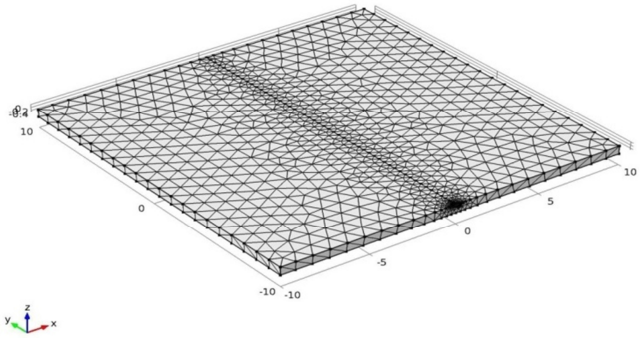

Figure 1(b). Fine mesh as generated by the COMSOL^R software.

The moving pulsed laser parameters used for the simulation are listed in Table 1 and Figure 1 (c).

Table 1 Geometrical and process parameters used for the simulation of scan speed.

Name	Expression	Value	Description
Lz	0.5[mm]	5.0E-4 m	slab thickness
L	20[mm]	0.02 m	slab size
sigy	0.2[mm]	2.0E-4 m	pulse y standard deviation
sigx	0.2[mm]	2.0E-4 m	pulse x standard deviation
Q0	100[W]	100 W	total laser power
Rc	0.5	0.5	reflection coefficient
Ac	0.02[1/cm]	2 1/m	absorbtion coefficient
x0	0[mm]	0 m	pulse center x coordinate
y0	-25[mm]	-0.025 m	pulse center y coordinate
W	20[mm]	0.02 m	slab width
v	100[mm/s]	0.1 m/s	laser velocity
omega	v/rad	2 1/s	angular velocity
time_end	W/v	0.2 s	last time step
time_step	time_end/500	4.0E-4 s	time step
rad	50[mm]	0.05 m	radius
pulse_width	10[ns]	1.0E-8 s	

Figure 1 (c) Snapshot from COMSOL^R for the geometrical and process parameters used in the simulation.

2.2 Mathematical Model

The heat equation is derived from the conservation of energy and Fourier's law of heat conduction, which states that the local heat flux is proportional to the negative of the gradient of the temperature. In a coordinate system that is fixed with the laser beam, the heat equation can be written as follows (Gospavic and Popov 2004).

$$\rho(x,T)c_p(x,T)\frac{\partial T(x,T)}{dt} - \nabla[k(x,T)\nabla T(x,T)] + \rho(x,T)c_p(x,T)v_s\nabla T(x,T) = Q(x,T) \quad (1)$$

Where ρ is the mass density of the material, c_p is the specific heat at constant pressure, k is the thermal conductivity, and v_s is the velocity of the substrate relative to the heat source. The left hand side of this heat equation describes the evolution of temperature due to heat conduction as well as the convective term, and v_s accounts for the shift in reference frame. The right hand side of this heat equation incorporates the contribution of heat sources and sinks through the volumetric heating rate $Q(x,T)$. The evolution of the temperature inside the material is initially driven by the volumetric heating term as well as the boundary conditions of the particular problem. Heat exchanges due to convection and radiation at the surface can be accounted for in the boundary conditions of the particular problem (Gospavic and Popov, 2004).

The governing equations for the incompressible Newtonian fluid flow and heat transfer in the molten material are defined by the following equations (Craciun, 2002).

For the mass conservation (incompressible fluid):

$$\vec{\nabla}\cdot\vec{u} = 0 \quad (2)$$

Where $\vec{\nabla}$ is the fluid velocity.

For the momentum conservation:

$$\rho_L\left(\frac{\partial\vec{u}}{\partial t} + \vec{u}\cdot\vec{\nabla}\vec{u}\right) = \vec{\nabla}\cdot\left(-P + \vec{u}\cdot\vec{\nabla}\vec{u}\right) + \rho_{L0}\left(1-\beta_t(T_c+T_l)\right)\vec{g} \quad (3)$$

Where the last term $\vec{g}$ is introduced to account for the natural convection within the melt pool.

For the energy conservation:

$$C_L\left(\frac{\partial T_l}{\partial t} + \vec{\nabla}(\vec{u}\,T_l)\right) = \vec{\nabla}\cdot(K_l\vec{\nabla}T_l) \quad (4)$$

where $\vec{u}$ is the velocity of the fluid, P is the pressure, $\rho_{L\,//}$ and $\rho_{L0\,//}$ are the densities of the molten material at temperatures T_l and T_m, respectively. β_t is the coefficient of thermal expansion, and C_L and K_l are the heat capacity and thermal conductivity of the liquid phase, respectively.

2.3 Boundery conditions

Three types of boundary conditions exist: the specified temperatures, the specified heat flux, and the convection conditions. In the first case, specified temperatures are taken into account by reducing the system equations. This is achieved through inserting the known nodal temperatures into the system equations. The latter two cases involve only elements that have surfaces (element faces) on the outside surface of the global volume. As an illustration, Figure 2(a) shows two brick elements that share a common face in an assembled finite element model. For convenience, the common face perpendicular to the x axis is taken. In Figure 2(b), the two elements are shown separately with the associated normal vector components identified for the shared faces.

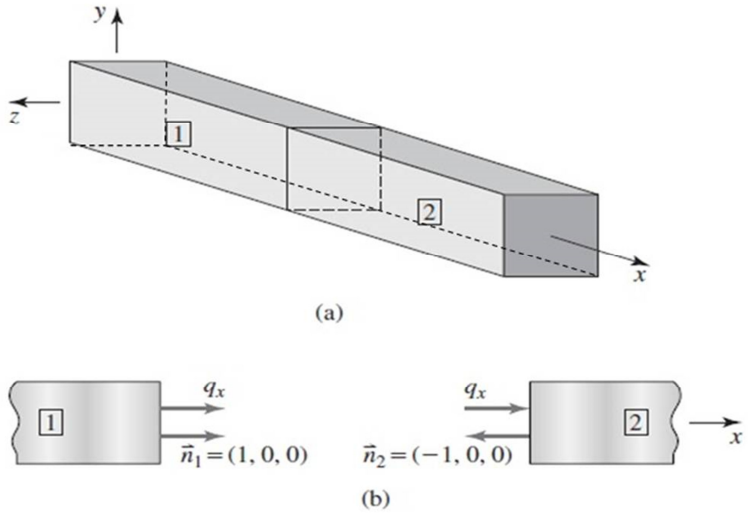

Figure 2 a. Common face in two 3-D elements. b. Edge view of common face.

1. Numerical Soulution Method

The two dimensional differential equations (1)-(4) associated with the boundary conditions and temperature field in the configuration were solved numerically using finite element analysis method..

A pulsed Nd:YAG laser with the wavelength of 1062nm was used for the machining simulation. The physical parameters for silicon investigated are listed in the Table 2.

Table 2 Physical Properties of Monocrystalline Silicon

Property, symbol (unit)	**Value**
Melting temperature, T_m (K)	1683
Normal boiling temperature, T_b (K)	3514
Critical point temperature, T_{cr} (K)	5159
Liquid density, ρ_l (kgm^{-3})	2520
Solid density, ρ_s (kgm^{-3})	2320
Latent heat of vaporization, L_v (J kg^{-1})	1.3722×10^7
Latent heat of fusion, L_m (J kg^{-1})	1.797×10^6
Liquid thermal conductivity, k_l (J cm^{-1} s K)	$0.5 + 2.9 \times 10^{-4}(T - T_m)$
Solid constant-pressure specific heat, C_{ps} (J g^{-1} K)	$0.694 \exp(2.375 \times 10^{-4} T)$
Liquid constant-pressure specific heat, C_{pl} (J g^{-1} K)	1050
Laser beam absorptivity for flat surface	0.66 for solid, 0.27 for liquid

2. Results and Discussion

In this section, a series of numerical simulations has been conducted to calculate the temperature distribution. Figures 4.1(a), 4.1(b), 4.1(c) and 4.1(d) show the surface temperatures of the material at the laser spot for the various scan speeds. The temperature rapidly increases during laser irradiation. For a scan speed of 100 mm/s, Figure 4.1(a), the maximum temperature of the center of the laser spot reaches 5300K which is beyond silicon critical temperature of 5159K. For a scan speed of 200 mm/s, Figure 5.1(b), the maximum temperature of the center of the laser spot reaches 4000K which is beyond silicon boiling temperature of 3514K. For a scan speed of 300 mm/s, Figure 4.1(c), the maximum temperature of the center of the laser spot reaches 3200K, which is below silicon boiling temperature of 3514K, but way above melting point of 1683K. For a scan speed of 400 mm/s, Figure 4.1(d), the maximum temperature of the center of the laser spot reaches 2500K, which is below silicon boiling temperature of 3514K, but above melting point of 1683K.

Figures 4.2(a), 4.2(b), 4.2(c) and 4.2(d) show the temperature distribution along the material thickness for the various laser scan speeds. Figures 4.3(a), 4.3(b), 4.3(c) and 4.3(d) show the kerf profile predictions along material thickness for different laser scan speeds.

For the scan speed of 100 mm/s, Figure 4.2(a), the temperature of the material below the beam spot (heating zone) reaches over 5200K. The whole thickness of the material at the heating zone is totally ablated. This region reaches temperatures over 2000K. This zone therefore experiences melting since the temperatures reached here surpass the silicon melting temperature of 1683K. The zone closest to the heating zone reaches temperatures over 3500K which is past silicon boiling point of 3514K. This prediction demonstrates that resulting kerf width would be greater than the beam spot diameter. The laser also cuts through the material thickness, as shownin Figure 4.3(a). This spot size would be useful for drilling and cutting through silicon by ablation.

For the scan speed of 200 mm/s, Figure 4.2(b), the temperature of the material below the beam spot reaches 4000K. The heating zone reaches boiling point and is partially ablated. The HAZ reaches temperatures up to 2000K. This zone therefore experiences partial melting since the temperatures reached here surpass the silicon melting temperature of 1683K. The partial boiling leads to bulge formation after resolidification, which leads to the decrease of kerf depth and kerf width. This prediction demonstrates that resulting kerf width would be smaller than the beam spot diameter. The laser also cuts through the material thickness, as shown in Figure 4.3(b). This spot size would be useful for drilling and cutting through silicon by ablation.

For the scan speed of 300 mm/s, Figure 4.2(c), the temperature of the material below the beam spot reaches 3400K. For the scan speed of 400 mm/s, the temperature of the material below the beam spot reaches 2800K. The heating zone reaches melting point but does not reach boiling point. The HAZ reaches temperatures up to 1500K, which is below the melting point of silicon. For both speeds, the laser does not cut through material thickness. The resulting kerf widths also would be smaller than the beam spot diameter, as shown in Figures 4.3(c) and 4.3(d) respectively. This scan speeds would be useful for microchannel creation in silicon.

Figure 4.4 shows the influence of laser scan speed on kerf depth. The kerf depth is seen to generally reduce as the scan speed increases. Figure 4.5 show the surface temperature at the laser spot for different scan

speeds. The temperature is seen to generally reduce as the scan speed increases. This reductions are to be expected since the laser used was a constant power pulsed laser, while the beam resident time at a spot reduced with increasing speed.

Figure 4.6 shows the temperature profile along the material depth for different scan speeds. The temperature is seen to generally reduce through the depth of the work piece. This reduction is to be expected since heat conduction takes place in the material.

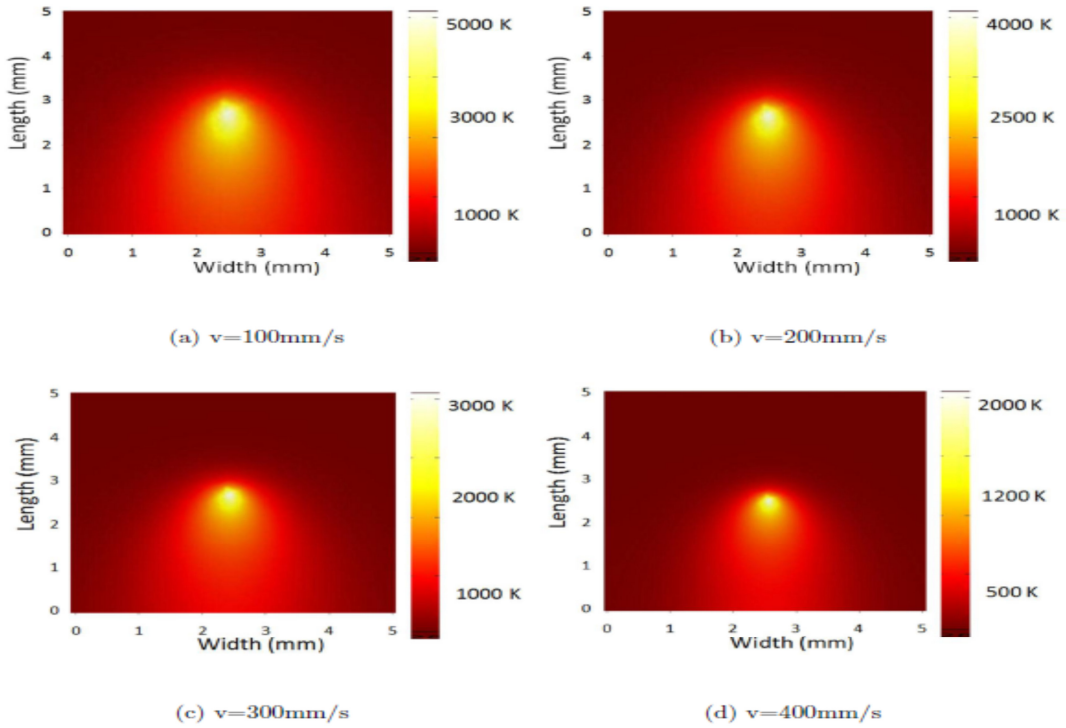

(a) v=100mm/s (b) v=200mm/s

(c) v=300mm/s (d) v=400mm/s

Figure 4.1: Surface temperatures of the material for different scan speeds.

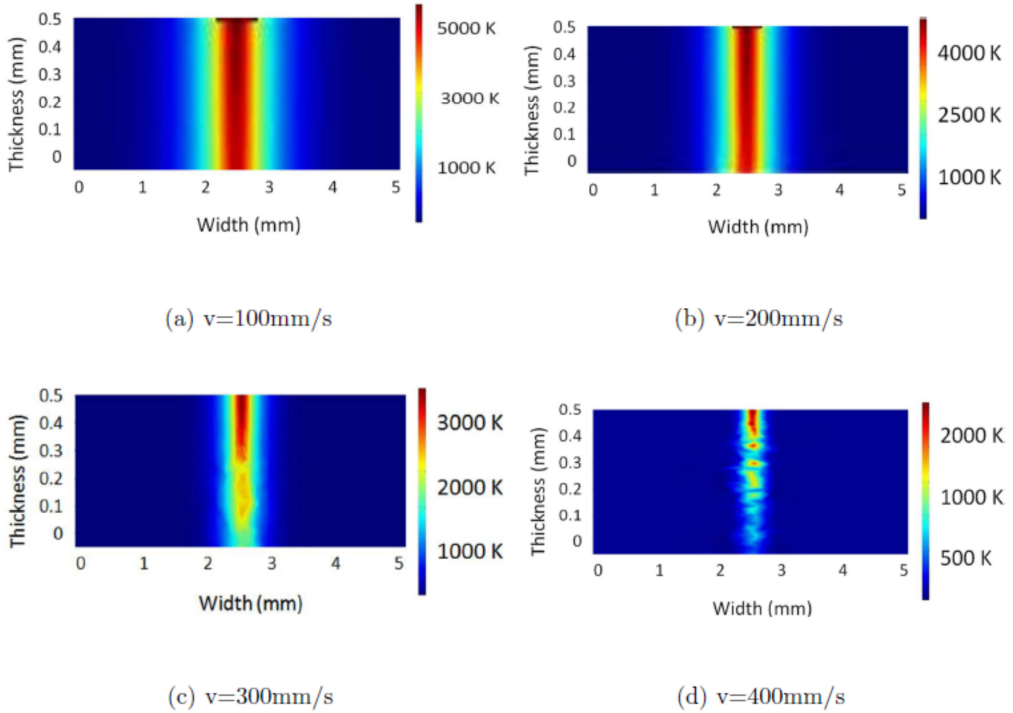

(a) v=100mm/s (b) v=200mm/s

(c) v=300mm/s (d) v=400mm/s

Figure 4.2: Temperature distribution along the material thickness for different scan speeds.

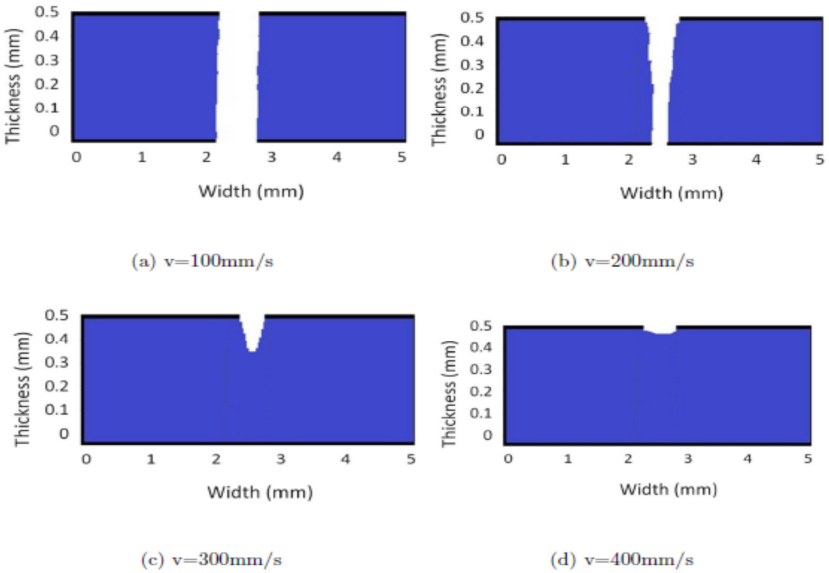

Figure 4.3: Kerf profile predictions along material thickness for different laser scan speeds.

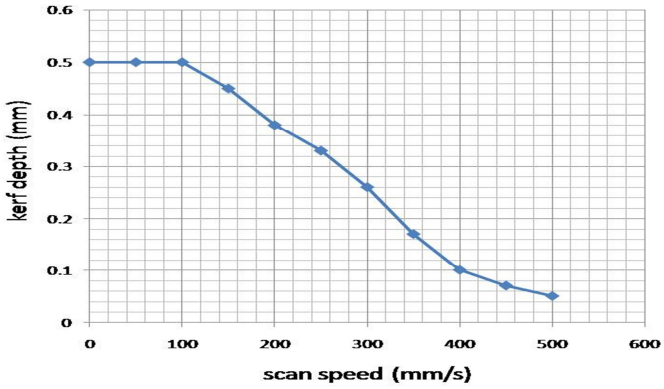

Figure 4.4: Influence of laser scan speed on kerf depth.

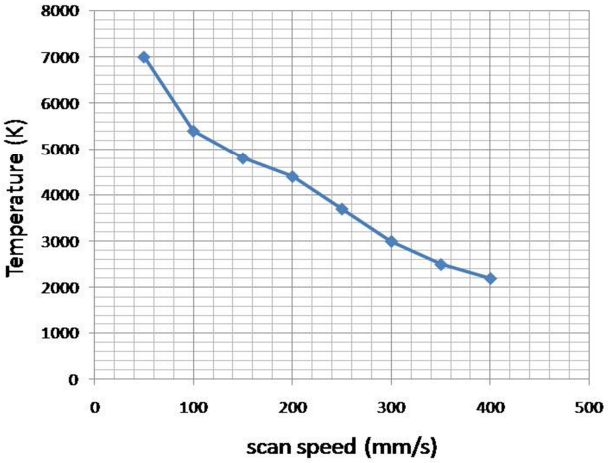

Figure 4.5: Surface temperature at laser spot for different scan speeds.

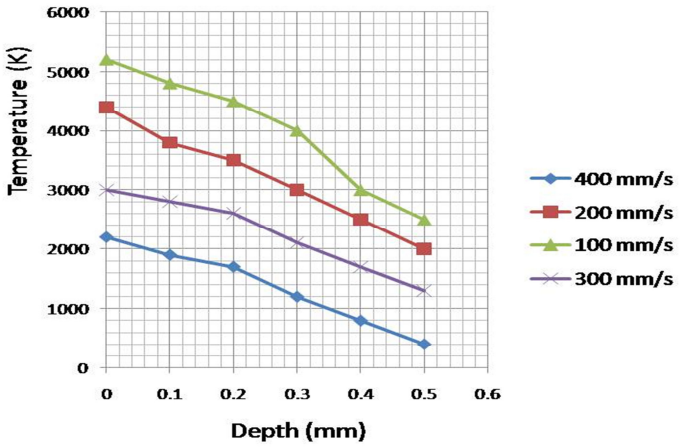

Figure 4.6: Temperature profile along depth for different scan speeds.

5. Conclusion

This work investigated the effect of laser scan speed on the kerf depth expected. A model for predicting the optimal laser scan speed for quality machining of silicon wafers was developed. The temperature distribution were evaluated using Finite Element Method. The mathematical equations for the simulation model were coded in the COMSOL^R software and the result images analyzed using IMAGEJ^R software.

On one hand, the results indicate that slow scan speeds result to melting and ablation in silicon. Slow speeds are optimal for applications such as drilling through holes, and trepanning of silicon wafers. On the other hand, high scan speeds result to minimal melting. High speeds are optimal for annealing and surface modification and texturization applications on monocrystalline silicon. Cutting quality is improved if scan speeds of the laser are chosen properly.

References

Brandi, F., Burdet, N., Carzino, R. and Diaspro, A. (2010). "Very large spot size effect in nanosecond laser drilling efficiency of silicon", *Laser Materials Processing* 30, 117-124.

Craciun, V. (2002). "Laser-induced explosive boiling during nanosecond laser ablation of silicon", *Journal of Applied Surface Science* 188, 288-292.

Gospavic, R. and Popov, V. (2004). "Modeling of laser material interaction using semi analytical approach", *Mathematics and Computers in Simulation* 65, 211-219.

Mazumder, J. and Steen, W. M. (1980). "Heat transfer model for CW material processing", *Journal of Applied Physics* 51(2), 941-947.

Modest, M. F. (1993). *Radiative Heat Transfer*. McGraw Hill.

Yilbas, B. S. (2004). "Laser cutting quality assessment and thermal efficiency analysis", *Journal of Materials Processing Technology* 155, 2106-2115.

Yu, L. (1997). "Three dimensional finite element method of laser cutting", *Journal of Materials Processing Technology* 63, 637-639.

The IISTE is a pioneer in the Open-Access hosting service and academic event management. The aim of the firm is Accelerating Global Knowledge Sharing.

More information about the firm can be found on the homepage:
http://www.iiste.org

CALL FOR JOURNAL PAPERS

There are more than 30 peer-reviewed academic journals hosted under the hosting platform.

Prospective authors of journals can find the submission instruction on the following page: http://www.iiste.org/journals/ All the journals articles are available online to the readers all over the world without financial, legal, or technical barriers other than those inseparable from gaining access to the internet itself. Paper version of the journals is also available upon request of readers and authors.

MORE RESOURCES

Book publication information: http://www.iiste.org/book/

Academic conference: http://www.iiste.org/conference/upcoming-conferences-call-for-paper/

IISTE Knowledge Sharing Partners

EBSCO, Index Copernicus, Ulrich's Periodicals Directory, JournalTOCS, PKP Open Archives Harvester, Bielefeld Academic Search Engine, Elektronische Zeitschriftenbibliothek EZB, Open J-Gate, OCLC WorldCat, Universe Digtial Library , NewJour, Google Scholar